



## Engineering oxygen vacancies and nickel dispersion on CeO<sub>2</sub> by Pr doping for highly stable ethanol steam reforming

Zhourong Xiao<sup>a</sup>, Yueling Li<sup>a</sup>, Fang Hou<sup>a</sup>, Chan Wu<sup>a</sup>, Lun Pan<sup>a,b</sup>, Jijun Zou<sup>a,b</sup>, Li Wang<sup>a,b</sup>, Xiangwen Zhang<sup>a,b</sup>, Guozhu Liu<sup>a,b</sup>, Guozhu Li<sup>a,b,\*</sup>

<sup>a</sup> Key Laboratory for Green Chemical Technology of Ministry of Education, School of Chemical Engineering and Technology, Tianjin University, Tianjin 300072, China

<sup>b</sup> Collaborative Innovation Center of Chemical Science and Engineering (Tianjin), Tianjin 300072, China



### ARTICLE INFO

#### Keywords:

Pr doping  
Oxygen vacancy  
Metal-support interaction  
Ethanol  
Steam reforming  
Hydrogen production

### ABSTRACT

Catalytic steam reforming of ethanol has drawn great attention for sustainable hydrogen production. This paper describes the development of various CeO<sub>2</sub> supported Ni catalysts for efficient steam reforming of ethanol. Different amounts of Pr were doped into ceria using a sol-gel strategy compared with the traditional impregnation method. The physicochemical properties of the fresh and spent catalysts, e.g., Ni dispersion, oxygen vacancies, and metal-support interaction, were well characterized by various techniques, including X-ray diffraction, N<sub>2</sub> adsorption-desorption, H<sub>2</sub> temperature-programmed reduction, H<sub>2</sub> chemisorption, Raman, electron paramagnetic resonance, X-ray photoelectron spectroscopy, transmission electron microscopy, and thermogravimetric analysis. Highly dispersed Ni nanoparticles, abundant oxygen vacancies and enhanced metal-support interaction have been achieved by properly doping of praseodymium (Pr) and the sol-gel preparation. The origin of abundant oxygen vacancies in Pr-doped CeO<sub>2</sub> supported Ni catalyst has been revealed by density functional theory (DFT) calculations. Active and stable steam reforming of ethanol have been achieved on CeO<sub>2</sub> supported Ni with suitable Pr doping. Complete conversion of ethanol has been maintained for more than 7200 min without any activity loss at 600 °C and atmospheric pressure with H<sub>2</sub>O/C<sub>2</sub>H<sub>5</sub>OH of 4 and C<sub>2</sub>H<sub>5</sub>OH-H<sub>2</sub>O gas hourly space velocity (GHSV) of 44,240 ml/g<sub>cat</sub> h<sup>-1</sup> when Ni was loaded on 20%-Pr doped ceria (10Ni-CePr<sub>0.20</sub>). The rate of coke deposition on the optimal catalyst was as low as 0.00056 g<sub>cat</sub>·h.

### 1. Introduction

Nowadays the quest for renewable, cheap and environmentally friendly energy sources to replace fossil fuels has captured much attention and has remained an ongoing challenge [1]. Because fossil fuels from limited sources produce large amounts of gas emissions such as NO<sub>x</sub>, SO<sub>x</sub> and inhalable particles resulting in a variety of serious environmental issues, such as ozone depletion, photochemical smog, and acid rain [2]. This critical situation has encouraged scientists to develop alternative processes to produce energy in a clean and viable way from an economic viewpoint [3]. Hydrogen is one of the cleanest energy carriers. For instance, proton exchange membrane fuel cells (PEMFC) using hydrogen for electricity generation only generate water [4]. Production of H<sub>2</sub> from natural sources, such as natural gas [5], bio-alcohols [6], is a competitive technology for alternative clean energy. Steam reforming of ethanol (SRE) for H<sub>2</sub> production has gained great attention, as shown in Eq. (1). Because ethanol is renewable, easy to be handled and transported, and thermodynamically feasible to be

decomposed. Moreover, ethanol with low toxicity offers smaller pollution to the environment as a sustainable source of energy [7–9].



In the past few years, the interests in developing hydrogen fuel cells have spurred extensively studies on the ESR process, especially the catalyst [7,10]. Noble metal catalysts can effectively break C–C and C–H bonds with a relatively good stability, but the high cost limits their large-scale application [11,12]. Nonprecious catalysts, especially Ni-based catalysts, are widely employed in the reforming process due to their low cost, wide availability and excellent capability for C–C and C–H bond cleavage [13–18]. Unfortunately, there exists severe deactivation due to large amount of coke deposited on Ni surface that can not be removed in time [19–22].

Numerous works have been carried out to develop active Ni-based catalysts with significant suppression of carbon deposition [23]. Gong et al. pointed out that manipulation of coke formation in the overall reforming reaction can be realized by modification of catalyst (e.g.,

\* Corresponding author.

E-mail address: [gzli@tju.edu.cn](mailto:gzli@tju.edu.cn) (G. Li).

type of active component and promoter) through identification of reaction pathways and key intermediates leading to carbonaceous deposits [6]. It is also proposed that trace noble metal could promote the stability of nickel based catalyst, which is due to a cooperative effect between noble metal and nickel that facilitates the gasification of carbon precursor. Noronha et al. showed that the addition of trace Pt reduced coke deposition via the hydrogenation of highly active carbon species adsorbed on the surface at a higher rate than carbon diffusion into bulk nickel [11]. It has been postulated that this process requires both the metal and oxide parts of the catalyst to work co-operatively, with the metal breaking C–C and C–H bonds of ethanol, and the oxide support promoting the dehydrogenation (or dehydration) as well as the dissociation of H<sub>2</sub>O [9,14,24]. Alkali, alkaline or transition metal oxides have been widely used to increase Ni activity and suppress coke [5,25–31]. Li et al. reported that ceria not only increased catalytic activity but also suppressed carbon deposition [27,28]. They attributed these positive effects to the oxidative properties of CeO<sub>2</sub> and enhanced Ni dispersion on CeO<sub>2</sub>. Another method is the addition of a second non-noble metal to form bimetal catalyst [31–33]. The synergistic effect of these two non-noble metals increases catalytic activity and coke resistance.

Moreover, Ni NPs have been confined in porous support, such as porous silica [15,26,27], alumina [29,34] and hydrotalcite-like materials [18], to improve Ni dispersion, suppress Ni sintering and reduce coke deposition. Ni-core-SiO<sub>2</sub>-shell or sandwiched Ni-core SiO<sub>2</sub>-shell structures have been developed with high resistance to both carbon deposition and metal sintering [17]. Additionally, various structures, like perovskite [16], spine [35], pyrochlore [36], solid solutions [5,14,37], has also been used to design new catalysts for the inhibition of coke deposition. Wang et al. showed that doping Pr into ceria lattice greatly promotes the redox property of the oxide support by creating more surface oxygen vacancies, resulting in high resistance of coke and good stability in SRE [38]. Previous reports also showed that solid solution possessing high dispersion of active species exhibits high catalytic activity and stability in steam reforming [16,37,39]. It is of great interest and importance to develop and investigate Pr doped Ni-CeO<sub>2</sub> solid oxide catalysts based on the combination of both strategies mentioned above. To the best of our knowledge, preparing solid oxide by sol-gel method and tuning metal-support interaction and oxygen vacancy concentration by Pr doping for CeO<sub>2</sub> supported Ni has not been reported in SRE.

Herein, we prepared and investigated various Pr-doped ceria supported Ni catalysts to achieve active and stable steam reforming of ethanol. The sol-gel method has been employed during catalyst preparation to finely tune its physicochemical properties for the developing of optimal Ni-Ce-Pr solid oxides. The experimental data of SRE on the as-synthesized catalysts was collected to evaluate their catalytic performance. A detailed investigation regarding the application of ceria supported Ni catalysts in SRE has been carried out. Moreover, DFT + U calculations were carried out to reveal the mechanism of oxygen vacancy formation in the catalysts. The structure of catalysts has been characterized in an attempt to establish a relationship between catalytic activity and stability and the structure of ceria supported Ni.

## 2. Experimental

### 2.1. Preparation of catalysts

Ceria supported Ni catalyst and Pr-doped ceria supported Ni catalyst were prepared by citric acid-assisted sol-gel method, which are denoted as 10Ni-CePr<sub>x</sub> (x = 0, 0.05, 0.10, 0.20 and 0.30), where x represents the amount of Pr doped into ceria. The weight percentage of Ni was set as 10 wt% in final catalyst. For example, 10Ni-CePr<sub>0.20</sub> means that the weight percentage of Ni is 10 wt%, the mole ratio of Pr (0.2) to Ce (0.8) is 1/4. For the synthesis of 10Ni-CePr<sub>0.20</sub>, Ni(NO<sub>3</sub>)<sub>2</sub>·6H<sub>2</sub>O (Tianjin Guangfu fine chemical research institute), Ce(NO<sub>3</sub>)<sub>3</sub>·6H<sub>2</sub>O (Beijing

HWRK Chem Co., LTD) and Pr(NO<sub>3</sub>)<sub>3</sub>·6H<sub>2</sub>O (Beijing HWRK Chem Co., LTD) with desired molar ratios were dissolved in deionized water and stirred for 30 min. Then, a concentrated solution of citric acid (Tianjin Guangfu fine chemical research institute) (molar ratio of citric acid: metal ion is 2:1) was prepared and added to the mixed nitrate solution. The resulting solution was heated to 60 °C and kept at this temperature for 12 h, followed by evaporating using a water bath. The viscous solution was then dried at 120 °C for 12 h, which resulted in a spongy solid. The obtained solids were grinded and calcined at 600 °C for 4 h. For easy comparison, traditional impregnation method was also employed to prepare Pr-doped ceria supported Ni catalyst, and the as-synthesized catalyst is denoted as 10Ni-CePr<sub>0.20</sub>-IMP. Firstly, solid support of Ce<sub>0.8</sub>Pr<sub>0.2</sub>O<sub>2</sub> was prepared using the citric acid-assisted sol-gel process. Then, the Ce<sub>0.8</sub>Pr<sub>0.2</sub>O<sub>2</sub> support was impregnated with a solution of Ni(NO<sub>3</sub>)<sub>2</sub>·6H<sub>2</sub>O (Tianjin Guangfu fine chemical research institute). The obtained slurry was stirred for 6 h and then slowly evaporated at 80 °C. Then, the mixture was dried at 120 °C for 24 h and calcined at 600 °C for 4 h. The samples of pure CeO<sub>2</sub> and NiO were prepared using a similar method to that of 10Ni-CePr<sub>0.20</sub>. The as-prepared catalysts were grinded and sieved to 20–40 mesh particles. After *in situ* reduction by H<sub>2</sub> with a flow rate of 50 ml/min at 500 °C for 1 h, reduced catalyst for catalytic tests was obtained.

### 2.2. Characterization

The BET surface areas of catalysts were measured using a Micromeritics Tristar 3000 analyzer by N<sub>2</sub> adsorption-desorption at –196 °C. Before analysis, the samples were degassed for 12 h at 200 °C under a vacuum. Specific surface area was calculated from the isotherm using the Brunauer-Emmett-Teller (BET) method. Pore size distribution and the cumulative volumes of pores were obtained by the Barrett-Joyner-Halenda (BJH) method from the desorption branches of the N<sub>2</sub> isotherms.

XRD characterization was performed with 2θ values between 20° and 85° using a Rigaku D8-Focus diffractometer employing the graphite filtered Cu K $\alpha$  radiation ( $\lambda = 1.54056 \text{ \AA}$ ).

Temperature-programmed reduction using hydrogen (H<sub>2</sub>-TPR) was conducted on an AMI-300 apparatus. For H<sub>2</sub>-TPR, a powder sample (100 mg) was pretreated at 400 °C for 1 h under flowing Ar (30 ml/min) to remove any moisture and impurities. After cooling to 100 °C, the gas of 10 vol% H<sub>2</sub>-Ar with a flow rate of 30 ml/min was introduced. Then the temperature was increased to 900 °C at a rate of 10 °C/min.

Temperature-programmed oxidation (TPO) was conducted on the AMI-300 apparatus. The experiments were performed in a flow of 5% vol% O<sub>2</sub>/Ar (50 ml/min) with a heating rate of 10 °C/min and a final temperature of 750 °C.

H<sub>2</sub> chemisorption was performed in an Autochem 2920 (Micromeritics). The catalyst was reduced at 500 °C for 1 h in a 10% H<sub>2</sub>/Ar flow. After adjusting the temperature of the catalyst bed to 50 °C, H<sub>2</sub> was added to the catalysts until H<sub>2</sub> saturation occurred. From the amount of chemisorbed H<sub>2</sub>, the Ni dispersion was calculated, assuming that the adsorption stoichiometry was one hydrogen atom for one surface Ni atom (H/Ni surface = 1).

TEM images were collected using a JEM-2100 F microscope. The samples were prepared by dropping and drying the reduced/spent catalyst, which had been dispersed in anhydrous ethanol by sonication, on holey carbon coated Cu grids. The Nano-measurer software (Fudan University, China) was adopted to calculate the average particle size of Ni on the fresh/spent catalysts. The average value of particle size was statistically calculated by the measurement of more than 100 particles in several selected TEM images. The scanning electron microscopy (SEM) images were obtained by FEI Nanosem 430.

Electron paramagnetic resonance (EPR) were obtained by Bruker E500 spectrometer at –196 °C.

Inductively coupled plasma (ICP) emission spectrometer was used in an Optima 5300DV (Perkin Elmer).

TG/DTG was carried out using a thermal analysis system (Q50-1688-TGA Instruments). The experiments were performed in a flow of air (50 ml/min) with a heating rate of 10 °C/min and a final temperature of 800 °C. The amount of carbon deposition was calculated based on the mass loss profiles in DTG test.

The X-ray photoelectron spectra (XPS) were recorded on an ESCALAB 250Xi spectrometer (Thermo Fisher Scientific) with an Al K $\alpha$  ( $h\nu = 1486.6$  eV) X-ray source. Charging effects were corrected by adjusting the binding energy of the C 1s peak from carbon contamination to 284.8 eV.

Raman spectra of the as-prepared/spent catalysts were collected on a DXR Microscope system. Sample of approximate 50 mg were excited using an argon laser operating at 532 nm.

### 2.3. Catalyst evaluation

Catalytic activity tests were conducted at atmospheric pressure in a stainless steel fixed-bed tubular reactor (6 mm ID) loaded with 300 mg catalysts (20–40 mesh). The catalyst mixed with 1.2 g of SiC to prevent catalyst moving in stainless steel tube reactor. Before the reaction, the sample was *in situ* reduced by H<sub>2</sub> with a flow rate of 50 ml/min at 500 °C for 1 h. To prevent initial coke deposition, N<sub>2</sub> (60 ml/min) and steam were introduced into the reactor for 15 min before introduction of ethanol solution. A premixed water-ethanol solution with water to ethanol molar ratio of 4:1 was fed into the reactor by an HPLC pump into the heated chamber (300 °C) to be evaporated completely. The total flow rate of the liquid of water-ethanol was 0.255 ml/min. Then the gaseous water/ethanol were mixed with the stream of N<sub>2</sub> (60 ml/min) in a mixer before entering the tubular reactor. Partial pressure of ethanol was maintained constantly at 15.73% for all the experiments. The introduced reaction gas mixture was composed of 21.33 vol% N<sub>2</sub> and 78.67 vol% ethanol-water. The gas hourly space velocity (GHSV) of ethanol and water was set to 44,240 ml/g<sub>cat</sub> h<sup>-1</sup>. The gas products were analyzed by an online gas chromatograph (Varian Micro-GC 490) equipped with TCD detectors and three columns. Activated alumina and PPU columns were used for light hydrocarbon and CO<sub>2</sub> analysis respectively. The 5 Å molecular sieve column was used for the analysis of H<sub>2</sub>, CO, CH<sub>4</sub>. The nitrogen flow rate in each steam reforming test was fixed. Thus, based on the content of nitrogen, it is able to calculate the yields of the H<sub>2</sub>, CO, CO<sub>2</sub> and CH<sub>4</sub> in each experiment. The overall experimental uncertainty of this system is approximately  $\pm 2.5\%$ . The conversion of ethanol, gas product composition was calculated using the parameters measured during the tests as our reported literature [37].

$$\text{Ethanol conversion (wt\%)} = \frac{F_{\text{CO}}^{\text{out}} + F_{\text{CO}_2}^{\text{out}} + F_{\text{CH}_4}^{\text{out}}}{F_{\text{ethanol}}^{\text{in}}} \times 100 \quad (2)$$

$$\text{Gas product rate } (\mu\text{mol}/\text{min}) R(H_2) = \frac{A_{H_2} \cdot f_{H_2}}{A_{N_2} \cdot f_{N_2}} \times R(N_2) \quad (3)$$

$$\text{Carbon balance (wt\%)} = \frac{F_{\text{ethanol}}^{\text{out}} + F_{\text{gas}}^{\text{out}}}{F_{\text{ethanol}}^{\text{in}}} \times 100 \quad (4)$$

$A_{H_2}$  is represented the peak area of hydrogen,  $f_{H_2}$  is represented the response factor of hydrogen, while  $R_{N_2}$  was the nitrogen flow rate and was fixed in each steam reforming test.

### 2.4. DFT calculations

In this section, we perform comparative study of the electronic structure of doped and non-doped ceria using both standard GGA-DFT and DFT + U methods. DFT has difficulties accurately representing the nature of 4f orbitals of cerium [40]. Therefore, we implemented the DFT + U approach. The DFT + U method introduces an on-site Coulombic interaction (U term) that penalizes non-integer occupation of localized orbitals, effectively penalizing delocalization of electrons. We

introduced a U term on the 4f orbitals of ceria to properly describe the localization of electrons in reduced cerium oxide (CeO<sub>2-x</sub>). We used a U value of 5.0 eV, which is consistent with values used in previous DFT studies of ceria [41,42]. Praseodymium (4f) and nickel (3d) were also implemented by the DFT + U approach, the U value for Pr is 4.5 eV [43], the U value for Ni is 5.0 eV [44].

Energy cutoff of 450 eV was used for the plane wave expansion of the PAW, k-point sampling of (2 × 2 × 1) as performed using the Monkhorst Pack scheme, with the third vector perpendicular to the surface. For the structure optimization, the ionic positions were allowed to relax until the Hellman-Feynman forces were less than 0.05 eV/Å. These values have been found to give good convergence for the quantities under consideration here.

Formation energy of the oxygen vacancy,  $E_f^{\text{vac}}$  is defined as the energy needed to remove an oxygen atom per cell in the form of the form of half oxygen molecules from CeO<sub>2</sub>(111) under the neutral condition.  $E_f^{\text{vac}}$  is formulated as below [43].

$$E_f^{\text{vac}} = E(\text{CeO}_{2-x}) + \frac{1}{2}E(\text{O}_2) - E(\text{CeO}_2)$$

All formation energies of the oxygen vacancy of doping systems (include Pr, Ni, Ni and Pr) were calculated using above equation. The oxygen vacancy is on ceria (111) surface.

## 3. Results and discussion

### 3.1. Characterization of the as-prepared catalysts

N<sub>2</sub> adsorption-desorption isotherms of the as-prepared catalysts are shown in Fig. S1a. All the catalysts display type IV isotherms possessing a H1 hysteresis loop, indicating the presence of characteristic mesoporous structure. Pore size distribution calculated from the desorption branches of the N<sub>2</sub> isotherms using BJH method reveals narrow pore size distribution of the catalysts as illustrated in Fig. S1b. The average pore size of these mesoporous materials ranges from 3.5 nm to 4.0 nm. The data of surface area, pore volume and average pore diameter are summarized in Table S1. All the catalysts possess similar pore volume and pore size. The BET surface area of 10Ni-CePr<sub>x</sub> is a litter higher than that of 10Ni-CePr<sub>0.20</sub>-IMP.

Wide-angle XRD patterns of the as-prepared materials are shown in Fig. 1a. All catalysts exhibited crystalline fluorite structure of ceria with the space group of Fm3m. Characteristic peaks corresponding to (111), (200), (220), (311), (222), (400), (331) and (420) planes were identified through the XRD database (JCPDS No. 43-1002). No peak associated with nickel oxides were found, indicating the high dispersion of NiO species in the 10Ni-CePr<sub>x</sub> catalysts, which benefits from the sol-gel method. Moreover, characteristic peaks of Pr<sub>2</sub>O<sub>3</sub> and PrO<sub>2</sub> were not observed for all samples, indicating Pr species were well doped into ceria lattice [2,37]. In comparison, 10Ni-CePr<sub>0.20</sub>-IMP exhibited additional diffraction peaks at 37.2° and 43.3°, which is attributed to the existence of nickel oxides. This result illustrates that big particles of nickel oxides were formed on 10Ni-CePr<sub>0.20</sub>-IMP with poor dispersion [27,29]. A decrease in lattice parameter for Pr doped ceria (Table S1) is observed. This is ascribed to the presence of a large number of Pr<sup>4+</sup> cations (0.96 Å) doped into ceria (Ce<sup>4+</sup> 0.97 Å). This phenomenon is also supported by a slight shift of the peak position of Pr-doped samples towards higher angle compared with that of pure ceria (Fig. 1b). After reduction by H<sub>2</sub>, wide-angle XRD patterns of the obtained catalysts were also collected and shown in Fig. 1c. All catalysts exhibited crystalline fluorite structure of ceria after reduction. The diffraction peak at 44.5°, which can be assigned as the characteristic peak of metallic Ni<sup>0</sup>, can be obviously observed for the sample of 10Ni-CePr<sub>0.20</sub>-IMP. The diffraction peak of Ni<sup>0</sup> for 10Ni-CePr<sub>x</sub> catalysts are much less obvious than that for 10Ni-CePr<sub>0.20</sub>-IMP, suggesting that small Ni particles are highly dispersed in the samples prepared by the sol-gel method. We speculate that many species with enhanced Ni-Ce metal-support

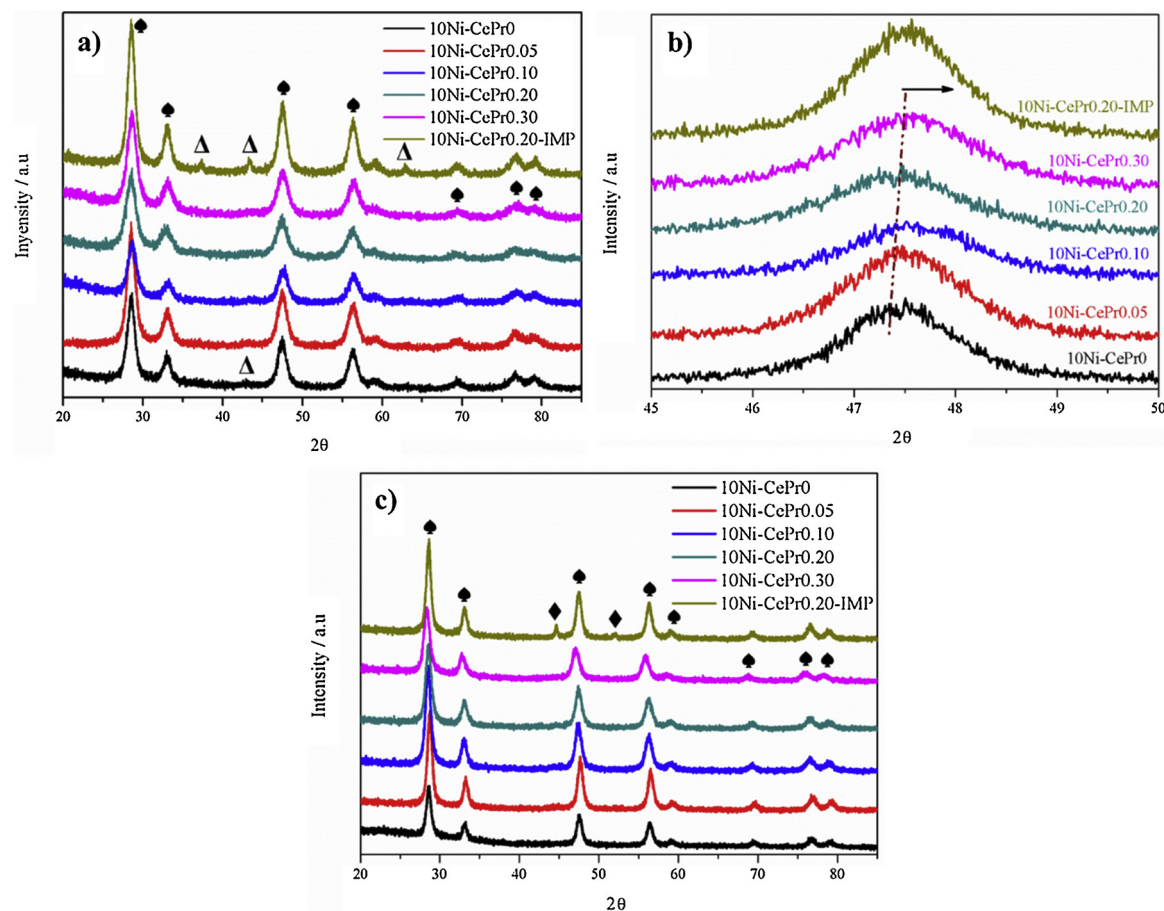


**Fig. 1.** Wide-angle XRD patterns of the as-prepared catalysts (a), the magnified view of the XRD patterns between 45° and 50° for the as-prepared catalysts (b) and the XRD patterns of the reduced catalysts (c). The peaks labeled by  $\blacktriangle$ ,  $\Delta$  and  $\blacklozenge$  are characteristic peaks of CeO<sub>2</sub>, NiO and Ni, respectively.

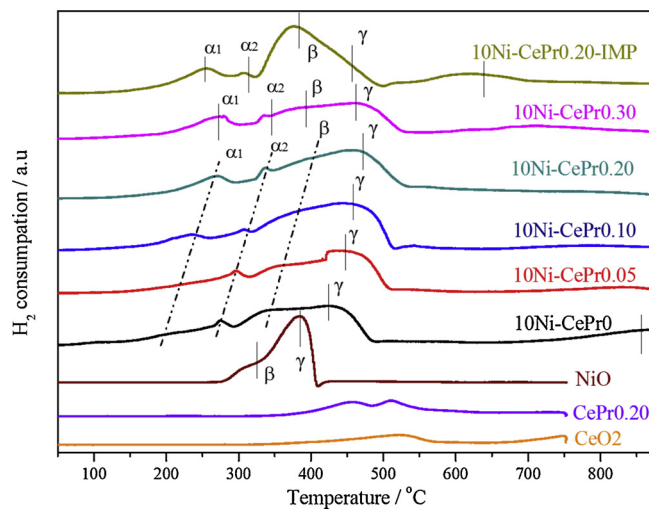


**Fig. 2.** TPR profiles of the as-prepared catalysts.

interaction were formed due to the fine distribution of constituents of the catalysts, which suppressed the aggregation of Ni nanoparticles during reduction. This hypothesis will be further verified by TPR analysis (Fig. 2).

The reduction behaviors of various Ni catalysts were measured by H<sub>2</sub>-TPR (Fig. 2). A crucial first evaluation on the feasibility of a material in practical application is to identify the degree of redox kinetics and the ability for oxygen mobility. According to previous reports, nickel oxides can be reduced to Ni<sup>0</sup> completely [14,45]. Therefore, H<sub>2</sub>

consumption peaks appearing at different temperatures represent different species with different interaction to the support [37,45–47]. For all the catalysts, four hydrogen consumption peaks ( $\alpha_1$ ,  $\alpha_2$ ,  $\beta$  and  $\gamma$ ) were observed. The peak at the temperature of higher than 700 °C and located at 525 °C are attributed to the reduction of lattice oxygen and surface oxygen of CeO<sub>2</sub> respectively [47]. For the Pr doped ceria (Ce<sub>0.8</sub>Pr<sub>0.2</sub>), the reduction temperature shifts to low temperature (455 and 511 °C), indicates easy reduction of oxygen species.  $\alpha_1$  and  $\alpha_2$  peaks can be ascribed to the reduction of adsorbed oxygen which is easily reduced by H<sub>2</sub> at low temperature.  $\beta$  and  $\gamma$  peaks are related to the reduction of nickel oxides [45,47,48].  $\beta$  peak is generally assigned to the reduction of relatively free nickel oxide that weakly interacts with the support surface. Whereas,  $\gamma$  peak is attributed to nickel oxides strongly interacting with ceria. All the four peaks of  $\alpha_1$ ,  $\alpha_2$ ,  $\beta$  and  $\gamma$  shift to higher temperature with the increasing of Pr dopant from 0 to 0.2 in 10Ni-CePr<sub>x</sub>, while the peaks shift a little to lower temperature when the doped Pr is further increased from 0.2 to 0.3. These results indicate that the content of doped Pr affects the interaction between nickel oxides and ceria. For the sample of 10Ni-CePr<sub>0.20</sub>-IMP, the main reduction peak is  $\beta$  peak. It indicates the presence of big particles of nickel oxides that weakly interact with the support. 10Ni-CePr<sub>0.20</sub> exhibited the highest NiO reduction temperature, indicating its enhanced metal-support interaction which is crucial to generate anti-sintering Ni particles during the reduction and reaction processes [27]. Moreover, the total peak area of  $\alpha_1$  and  $\alpha_2$  increases with the doping of more Pr, indicating enriched oxygen vacancies in the catalyst which is highly desired for coke inhibition [38].

Composition of the as-prepared catalysts was measured by ICP, the results are shown in Table 1. The real composition of the as-prepared

**Table 1**

Composition, Ni dispersion and Ni particle size of the as-prepared catalysts.

Catalysts	Ni (wt%) <sup>a</sup>	Ce (wt%) <sup>a</sup>	Pr (wt%) <sup>a</sup>	Ni surface area (m <sup>2</sup> /g <sub>Ni</sub> )	Ni dispersion (%) <sup>d</sup>	Ni particle size (nm) <sup>e,f</sup>
10Ni-CePr0	9.92	90.08	–	12.6 <sup>b</sup> /8.7 <sup>c</sup>	12.5	7.7 <sup>e</sup> /11.2 <sup>f</sup>
10Ni-CePr0.05	9.96	84.81	5.23	14.4	13.9	6.7
10Ni-CePr0.10	9.95	80.10	9.95	15.9	14.8	6.1
10Ni-CePr0.20	9.97	69.92	20.11	18.6 <sup>b</sup> /15.6 <sup>c</sup>	16.6	5.2 <sup>e</sup> /6.2 <sup>f</sup>
10Ni-CePr0.30	9.93	60.05	30.02	13.8	13.1	7.0
10Ni-CePr0.20-IMP	9.91	79.43	10.66	7.8 <sup>b</sup> /5.4 <sup>c</sup>	6.7	12.5 <sup>e</sup> /17.8 <sup>f</sup>

<sup>a</sup> Results from ICP tests.<sup>b</sup> Ni surface area of fresh catalyst calculated from the equation of  $9.7/d_{Ni} \times 10$ .<sup>c</sup> Ni surface area of spent catalyst calculated from the equation of  $9.7/d_{Ni} \times 10$ .<sup>d</sup> Data estimated from H<sub>2</sub>-chemisorption = Ni atoms on the surface/Total Ni atoms.<sup>e</sup> Average Ni particle size of fresh catalyst measured from TEM images.<sup>f</sup> Average Ni particle size of spent catalyst measured from TEM images.**Table 2**Relative proportion of different types of oxygen defects and the relative Ce<sup>3+</sup> ratio for the as-prepared catalysts.

Catalysts	F <sub>2g</sub>	O <sub>v</sub> + O <sub>h</sub>	(O <sub>v</sub> + O <sub>h</sub> ) /F <sub>2g</sub>	O <sub>II</sub> /(O <sub>I</sub> + O <sub>II</sub> )	Ce <sup>3+</sup> /(Ce <sup>3+</sup> + Ce <sup>4+</sup> )
10Ni-CePr0	51.23	48.77	0.952	0.478	0.252
10Ni-CePr0.05	48.67	51.33	1.055	0.501	0.311
10Ni-CePr0.10	40.26	59.74	1.484	0.512	0.362
10Ni-CePr0.20	36.97	63.03	1.704	0.535	0.397
10Ni-CePr0.30	33.21	66.79	2.011	0.539	0.341
10Ni-CePr0.20-IMP	30.65	69.35	1.588	0.521	0.321

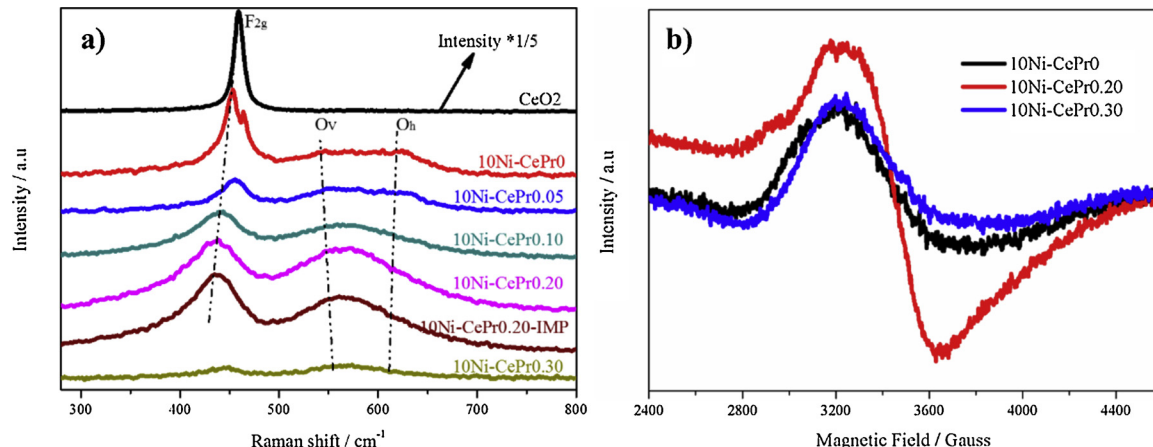


Fig. 3. a) Raman profiles and b) low temperature EPR spectra of the as-prepared catalysts.

catalysts is close to the theoretical value. Ni surface area was calculated from the equation of  $9.7/d_{Ni} \times 10$ , in which  $d_{Ni}$  was measured from corresponding TEM images (Fig. S2). The average Ni particle size of 10Ni-CePr<sub>0</sub> is centered at 7.7 nm and corresponding Ni surface area is 12.6 m<sup>2</sup>/g. Moreover, with the increased content of Pr dopant from 0 to 0.2 (10Ni-CePr<sub>x</sub>,  $x \leq 0.2$ ), the particle size of Ni is reduced and corresponding Ni surface area is increased. When the doped Pr is further increased to 0.3 (10Ni-CePr<sub>0.30</sub>), the particle size of Ni is increased to 7.0 nm and the Ni surface area is decreased to 13.8 m<sup>2</sup>/g. The catalyst of 10Ni-CePr<sub>0.20</sub> possesses the smallest Ni particle size (5.2 nm) and the highest Ni surface area (18.6 m<sup>2</sup>/g). In comparison, 10Ni-CePr<sub>0.20</sub>-IMP possessed larger Ni particle with broad distribution, in which the Ni surface area (7.8 m<sup>2</sup>/g) is less than half of 10Ni-CePr<sub>0.20</sub>. These results illustrate that suitable content of Pr doped by the sol-gel method can effectively decrease Ni particles size and increase Ni surface area of the catalyst. It is in good agreement with the analyses based on XRD (Fig. 1) and TPR (Fig. 2). Highly dispersed nickel oxides with enhanced interaction with support prevent their aggregation during the harsh reduction process. Therefore, catalysts prepared by the sol-gel method can maintain smaller Ni particle size with higher surface area (Table 2).

Similarly, previous study also showed that larger interface between nickel and ceria facilitates oxygen transfer and enhances dissociation of water [14,24].

HRTEM image of the reduced 10Ni-CePr<sub>0.20</sub> is displayed in Fig. S2g. The (111) planes of CeO<sub>2</sub> were mainly observed, and Ni (111) planes were present in the tiny nickel nanoparticles. Corresponding EDX spectrum of the reduced 10Ni-CePr<sub>0.20</sub> shows intense peaks of Ce, Pr and Ni (Fig. S2i). The distribution of Ni, Ce, Pr and O elements on 10Ni-CePr<sub>0.20</sub> was also characterized by EDS-mapping technology, and the results are shown in Fig. S3. All the elements are well distributed, which further confirms our conclusion that small particles of Ni are highly dispersed on Pr-doped ceria. H<sub>2</sub>-chemisorption was carried out to evaluate the dispersion of nickel particles, and the results are also listed in Table 1. The trend of Ni dispersion observed among all the samples is similar to the results from TEM images. 10Ni-CePr<sub>0.20</sub> showed the highest Ni dispersion (16.6%), while 10Ni-CePr<sub>0.20</sub>-IMP possessed very low dispersion of Ni (6.7%).

Raman spectroscopy is a powerful technique to analyze structural properties of ceria nanomaterials due to its strong sensitivity of phonon characteristics to the crystalline nature. Raman spectra of all the as-

synthesized samples are displayed in Fig. 3a. The spectrum of  $\text{CeO}_2$  shows a main band located at  $465\text{ cm}^{-1}$ , which is attributed to the  $F_{2g}$  vibrational mode of the cubic fluorite-type structure of cerianite [49]. A red shift and an asymmetrical broadening of the peak have been observed in the spectra of the Pr-doped catalysts in comparison with the catalyst using bare  $\text{CeO}_2$ . Specially, the  $F_{2g}$  vibrational mode peak of  $10\text{Ni-CePr}_{0.20}$  is located at  $438.6\text{ cm}^{-1}$ , indicating that more Ni or Pr was doped into ceria lattice. Previous report showed that high concentration of doped hetero-ion led to the shift of  $F_{2g}$  mode energy to lower frequencies [50]. Niu et al. even pointed out that the systematic peak shift was mainly attributed to the expansion of lattice and the peak broadening was related to the generation of defects, both of which were caused by Pr-doping and responsible for the progressive reduction of  $F_{2g}$  Raman mode intensity [51]. The  $F_{2g}$  peak intensity of  $10\text{Ni-CePr}_{0.30}$  is very weak, which indicates large Pr doping probably leads to a stronger fluorescence effect that reduces the detectable Raman signal [51]. Previous report showed that  $\text{Pr}^{3+}$  doping gradually destroys the fluorite ( $\text{CeO}_2$ ) symmetry and eventually leads to reduces the intensity of  $F_{2g}$  peak [52]. Two other Raman modes at  $550\text{ cm}^{-1}$  and  $610\text{ cm}^{-1}$  originate from defect structures in the lattice [49,53]. The band at  $550\text{ cm}^{-1}$  ( $\text{O}_v$ ) is ascribed to the formation of extrinsic oxygen vacancies via the substitution of  $\text{Ce}^{4+}$  ion by  $\text{Pr}^{3+}$  ion in order to maintain electrostatic charge neutrality in the ceria lattice. The band at  $610\text{ cm}^{-1}$  ( $\text{O}_h$ ) is attributed to the presence of intrinsic oxygen vacancies arising from lattice expansion and/or distortion due to ionic radii disparity between  $\text{Ce}^{4+}$  and  $\text{Pr}^{4+}/\text{Pr}^{3+}$  [49]. As shown in Fig. 3 and Table 2, the values of  $(\text{O}_v + \text{O}_h)/\text{F}_{2g}$  are continuously increased from 0.952 to 2.011 with the increasing of Pr content from 0 to 0.3. The values of  $(\text{O}_v + \text{O}_h)/\text{F}_{2g}$  for  $10\text{Ni-CePr}_{0.20}$ -IMP is 1.588 which is smaller than that of  $10\text{Ni-CePr}_{0.20}$  (1.704). Therefore, the defects in the lattice can be effectively created by both Pr doping and the sol-gel preparation.

Moreover, the EPR signal ( $g = 2.003$ ) of Ni and Pr co-doped ceria is symmetrical, which is originated from the unpaired electrons at the oxygen vacancy sites [54], as shown in Fig. 3b. The highly intensive signal of  $10\text{Ni-CePr}_{0.20}$  suggests its more abundant oxygen vacancies than those of  $10\text{Ni-CePr}_0$  and  $10\text{Ni-CePr}_{0.30}$ . If the content of doped Pr is too high, e.g.  $10\text{Ni-CePr}_{0.30}$ , the ratio of  $\text{Ce}^{3+}$  will be reduced due to the substitution of more Ce by Pr. These results are in good agreement with Raman analysis. XPS will be employed to further confirm our conclusion, and the results of  $\text{O}_{\text{II}}/(\text{O}_{\text{I}} + \text{O}_{\text{II}})$  and  $\text{Ce}^{3+}/(\text{Ce}^{3+} + \text{Ce}^{4+})$  will also be discussed in latter section.

Fig. S4a shows the XPS spectra of Ce 3d for the as-prepared catalysts. The two groups of spin orbital multiplets, corresponding to  $3d_{3/2}$  and  $3d_{5/2}$ , are denoted as U and V, respectively. For all the samples, there are three main  $3d_{3/2}$  peaks at about 901.3 (U), 908.1 (U<sub>2</sub>), and 917.1 (U<sub>3</sub>) eV and three main  $3d_{5/2}$  peaks at about 882.8 (V), 888.1 (V<sub>2</sub>), and 898.1 (V<sub>3</sub>) eV, all of which are attributed to the existence of  $\text{Ce}^{4+}$  state. The peaks at around 886.2 eV (V<sub>1</sub>) and 904.0 eV (U<sub>1</sub>) are hardly observed. Deconvolution of the spectra was carried out to determine the areas of V<sub>1</sub> and U<sub>1</sub> for the calculation of corresponding  $\text{Ce}^{3+}$  content. The results indicate co-existence of  $\text{Ce}^{3+}$  and  $\text{Ce}^{4+}$  species on the surface of all catalysts. The presence of  $\text{Ce}^{3+}$  ions in ceria lattice can maintain electrostatic equilibrium and generate oxygen vacancies. Previous study showed that the formation of  $\text{Ce}^{3+}$  ions is closely associated with the oxygen vacancies in ceria [53,54]. Wang et al. reported that  $\text{Ce}^{3+}$  content can be estimated from the area of U<sub>1</sub> and V<sub>1</sub> according the equation of  $\text{Ce}^{3+}(\%) = \frac{S_{V_1} + S_{U_1}}{\sum(S_{V_1} + S_{U_1})} \times 100$  [34]. Relative contents of  $\text{Ce}^{3+}$  have been calculated and summarized in Table 2. Initial doping of small amount of Pr into  $\text{CeO}_2$  ( $\text{Pr} \leq 0.2$ ) increases the percentage of  $\text{Ce}^{3+}$ . While, too much Pr ( $\text{Pr} = 0.3$ ) doped into ceria reduces the ratio of  $\text{Ce}^{3+}$ . This may be attributed to substitution of some  $\text{Ce}^{4+}$  by  $\text{Pr}^{4+}$  or partially substitution of  $\text{Ce}^{3+}$  by  $\text{Pr}^{3+}$  on ceria surface. These results are consistent with the EPR analysis (Fig. 3b).

The as-prepared catalysts exhibited  $\text{Ni}(2+)$   $2p_{3/2}$  peak at

$856.3 \pm 0.1\text{ eV}$  with satellite at  $862.1\text{ eV}$ . The higher energy pairs of the doublets characteristic to Ni 2p core level region were detected at  $872.8\text{ eV}$  for oxidized Ni species. As shown in Table S3, the content of nickel species in  $10\text{Ni-CePr}_{0.20}$ -IMP detected by XPS was higher than those samples prepared by the sol-gel method. It indicates that NiO particles were mainly distributed on the surface of support after the impregnation process, while embedment of NiO particles happened during the sol-gel preparation.

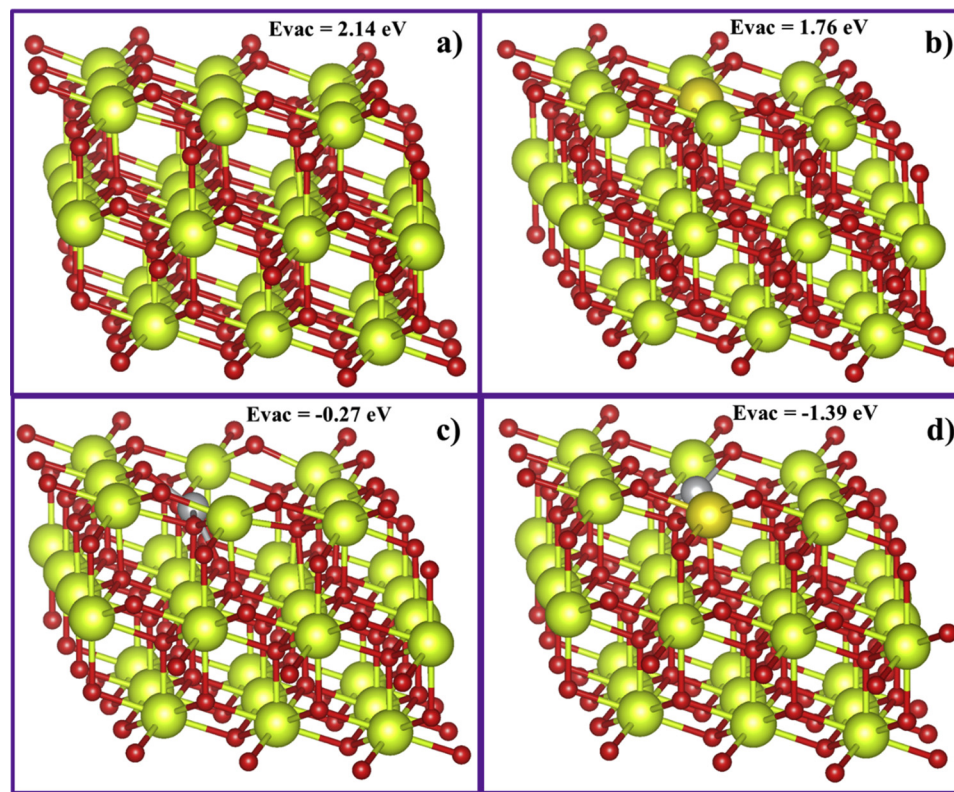
Fig. S4c presents the O1 s region of XPS spectra, in which two peaks can be clearly resolved. The peak at lower binding energy of  $529.2 \pm 0.1\text{ eV}$  is labeled as  $\text{O}_{\text{I}}$ , and the other peak at higher binding energy of  $531.3 \pm 0.2\text{ eV}$  is labeled as  $\text{O}_{\text{II}}$ . The  $\text{O}_{\text{I}}$  peak originates from  $\text{O}_2$  ions in the lattice [53]. The  $\text{O}_{\text{II}}$  peak, containing  $\text{O}_{\alpha}$  and  $\text{O}_{\beta}$  peaks, is controversial, since it has been assigned to the oxygen in the form of OH group or  $\text{O}^{2-}$  species [45,47]. This peak can be also associated with the presence of oxygen vacancies. Shah et al. concluded that  $\text{O}_{\text{I}}$  peak belongs to the oxygen in  $\text{O-Ce}^{4+}$  bond, whereas  $\text{O}_{\text{II}}$  peak originates from the oxygen in  $\text{O-Ce}^{3+}$  structure [37]. Previous report showed that the increased ratio of  $\text{O}_{\text{II}}$  could effectively enhanced the stability of catalyst [49]. Relative  $\text{O}_{\text{II}}(\text{O}_{\alpha} + \text{O}_{\beta})$  ratio was calculated and given in Table 2. Pr doping can constantly increase the ratio of  $\text{O}_{\text{II}}$ , and the sol-gel preparation method can further elevate  $\text{O}_{\text{II}}/(\text{O}_{\text{I}} + \text{O}_{\text{II}})$  to a higher value. The trends of  $\text{O}_{\text{II}}/(\text{O}_{\text{I}} + \text{O}_{\text{II}})$  in various catalysts are similar to those of  $(\text{O}_v + \text{O}_h)/\text{F}_{2g}$  calculated from Raman spectra (Fig. 3a).

Fig. S4d shows the Pr 3d spectra with two spin-orbit doublets. The peaks at the binding energies of  $929/949\text{ eV}$  and  $933/954\text{ eV}$  were labeled as a/a' and b/b', which can be assigned to  $\text{Pr } 3d_{5/2}$  (a, b) and  $\text{Pr } 3d_{3/2}$  (a', b') respectively. Doublets of a/a' and b/b' are present in both  $\text{PrO}_2$  and  $\text{Pr}_2\text{O}_3$  compounds [37]. With the increase of Pr doping, the peak intensities of both a/a' and b/b' were increased, indicating that Pr species were successfully doped into ceria.

The redox behavior of various ceria surface (bare  $\text{CeO}_2$ , Pr-doped  $\text{CeO}_2$ , Ni-doped  $\text{CeO}_2$  and Ni-Pr-co-doped  $\text{CeO}_2$ ) was investigated by a DFT + U method [42,43]. The DFT + U method introduces an on-site coulombic interaction (U term) that penalizes non-integer occupation of localized orbitals, effectively penalizing delocalization of electrons. U term on the 4f orbitals of ceria was introduced in order to precisely describe the localization of electrons in cerium oxide, and more details are described in experimental section. Perfect structures of different ceria (111) surfaces were firstly optimized, and the results are shown in Fig. S5. Previous results showed that doping hetero-ion could promote oxygen donation by lowering the energy that is necessary to be overcome for the formation of surface anionic vacancies [42]. With the effectively oxidation of deposited coke by surface anionic vacancies, the long-time stability of the catalyst can be greatly enhanced. The structures of different ceria (111) surfaces with oxygen vacancies near the doped atoms were also optimized. Then, formation energies of oxygen vacancies for our catalysts were calculated. The results are shown in Fig. 4 and corresponding values are summarized in Table S2. The order of formation energies of oxygen vacancies for different materials is  $\text{CeO}_2(111) > \text{Pr-CeO}_2(111) > \text{Ni-CeO}_2(111) > \text{Ni-Pr-CeO}_2(111)$ . For pure ceria (111), the formation energy of oxygen vacancies is  $2.14\text{ eV}$ , which is consistent with the results reported previously [40,42]. On the surface of Pr and Ni co-doped ceria this barrier can be effectively reduced. The formation energy of oxygen vacancies on  $\text{Ni-Pr-CeO}_2(111)$  is only  $-1.39\text{ eV}$ , indicating that solid solution of Ni, Pr co-doped ceria readily generates oxygen vacancies. Thus, the conclusion obtained based on experimental data of Raman (Fig. 3a), EPR (Fig. 3b) and XPS (Fig. S4c and Table 2) can be properly explained.

### 3.2. Catalytic performance tests

The initial catalytic activity of all the samples was firstly evaluated, aiming to figure out the role of Pr doping on  $\text{CeO}_2$  supported Ni. The effect of reaction temperature on the reforming reaction was revealed by the experimental data in Fig. S6a and Table S4. On all the catalysts,



**Fig. 4.** Various structures with oxygen vacancies and corresponding formation energies. a)  $\text{CeO}_2$ -vac, b)  $\text{Pr-CeO}_2$ -vac, c)  $\text{Ni-CeO}_2$ -vac and d)  $\text{Ni-Pr-CeO}_2$ -vac. The light yellow, deep yellow, red, and gray spheres, respectively, represent Ce atoms, Pr atoms, O atoms, and Ni atoms (For interpretation of the references to colour in this figure legend, the reader is referred to the web version of this article).

the conversion of ethanol was raised significantly by increasing reaction temperature, reflecting the endothermic feature of the reforming reaction. The catalysts prepared by sol-gel method show higher activity (Table S4) than that synthesized via conventional impregnation (10Ni-CePr<sub>0.20</sub>-IMP). Moreover, higher ethanol conversion was achieved over all Pr-doped catalysts (10Ni-CePr<sub>x</sub>,  $x > 0$ ) in comparison with that without any Pr (10Ni-CePr<sub>0</sub>). Specially, the initial of ethanol conversion of different catalysts are in the order of 10Ni-CePr<sub>0.20</sub> > 10Ni-CePr<sub>0.10</sub> > 10Ni-CePr<sub>0.02</sub> > 10Ni-CePr<sub>0.30</sub> > 10Ni-CePr<sub>0.20</sub>-IMP which is consistent with the Ni surface area and Ni particle size data. The formation rate of H<sub>2</sub> increased with the increasing of reaction temperature (Table S4), which can be explained by the fact that high temperature favors the formation of H<sub>2</sub> [27]. The catalyst prepared by sol-gel method show higher H<sub>2</sub> formation rate than that prepared by traditional impregnation method (10Ni-CePr<sub>0.20</sub>-IMP). The trend of the catalytic performance matches well with that of the dispersion of Ni particles, the status of metal-support interaction and the concentration of oxygen vacancies in these catalysts.

The initial activity of some catalysts and corresponding product distribution were measured at 550 °C, as shown in Fig. S6b-d. The conversion of ethanol over 10Ni-CePr<sub>0.20</sub> is more than 90% and corresponding hydrogen production rate is close to 6000 μmol/min during the test period of 180 min. In comparison, 10Ni-CePr<sub>0</sub> exhibited lower activity with similar product composition, as shown in Fig. S6d. For 10Ni-CePr<sub>0.20</sub>-IMP, after 60 min reaction, only 70.2% of ethanol was converted and the hydrogen production rate is less than 4350 μmol/min. This is attributed to its big Ni particle size with small Ni surface area and weak metal-support interaction, as shown in previous characterization. In the case of 10Ni-CePr<sub>0.20</sub> catalyst, Ni particles on Pr-doped ceria were with small particle size (5.2 nm), high Ni surface area (18.6 m<sup>2</sup>/g) and dispersion (16.6%). Moreover, 10Ni-CePr<sub>0.20</sub> possessed the highest ratio of Ce<sup>3+</sup> and oxygen vacancies, which is verify by EPR (Fig. 4b), XPS (Fig. S4c) and DFT calculations. With the increasing of doped Pr to 0.3 (10Ni-CePr<sub>0.30</sub>), the metal-support interaction is weakened and the concentration of oxygen vacancies is sharply reduced.

Thus, both ethanol conversion and hydrogen production rate over 10Ni-CePr<sub>0.30</sub> were decreased.

The catalysts of 10Ni-CePr<sub>0</sub> and 10Ni-CePr<sub>0.20</sub> were further evaluated at higher GHSV of 66,360 ml/g<sub>cat</sub> h<sup>-1</sup>, as shown in Fig. S6e and S6f. During the period of 1500 min, 10Ni-CePr<sub>0.20</sub> exhibited extraordinary performance with higher ethanol conversion and hydrogen production rate compared with 10Ni-CePr<sub>0</sub>. It indicates that doped Pr could highly affect the activity and stability of CeO<sub>2</sub> supported Ni for SRE.

Stability of all the catalysts was measured for a period of 3000 min (Fig. 5). The stability test was carried out under H<sub>2</sub>O/C<sub>2</sub>H<sub>5</sub>OH ratio of 4 and GHSV of 44,240 ml/g<sub>cat</sub> h<sup>-1</sup> at 600 °C and atmospheric pressure. Over the bare Pr-doped ceria support, Ce<sub>0.8</sub>Pr<sub>0.2</sub>O<sub>2</sub>, the conversion of ethanol was less than 70% and the average hydrogen production rate was less than 1500 μmol/min (Fig. S7). The main products were ethene and methane with a trace of CO detected. Steam reforming reaction scarcely happened over Ce<sub>0.8</sub>Pr<sub>0.2</sub>O<sub>2</sub>. The main reaction occurring on Ce<sub>0.8</sub>Pr<sub>0.2</sub>O<sub>2</sub> are ethanol dehydration and thermal cracking. With the loading of Ni on the support, steam reforming mainly proceeded. As shown in Fig. 5, catalysts prepared by the sol-gel method (10Ni-CePr<sub>x</sub>) exhibited higher activity and stability than that synthesized via conventional impregnation (10Ni-CePr<sub>0.20</sub>-IMP). On 10Ni-CePr<sub>0.20</sub>-IMP the initial ethanol conversion was 91.9%. With the increase of reaction, the conversion of ethanol declined quickly, which dropped to only 36.9% after 120 min. The hydrogen production rate decreased from 6906.7 μmol/min to 2398.5 μmol/min during this period. Deactivation of 10Ni-CePr<sub>0.20</sub>-IMP in SRE can be ascribed to the sintering of active metal and severe coke deposition. 10Ni-CePr<sub>0</sub> also lost its activity quickly (Fig. 5a). The conversion of ethanol was decreased gradually from 95.7% to 77.2%, and hydrogen production rate was reduced from 6940.5 μmol/min to 5907.2 μmol/min eventually after 3000 min. With the doping of Pr into CeO<sub>2</sub> supported Ni, the obtained catalysts showed enhanced performance in SRE. On 10Ni-CePr<sub>0.05</sub>, 100% conversion of ethanol was reached for up to 2280 min, and the final hydrogen production rate was 6943.9 μmol/min. With the increasing of doped Pr to

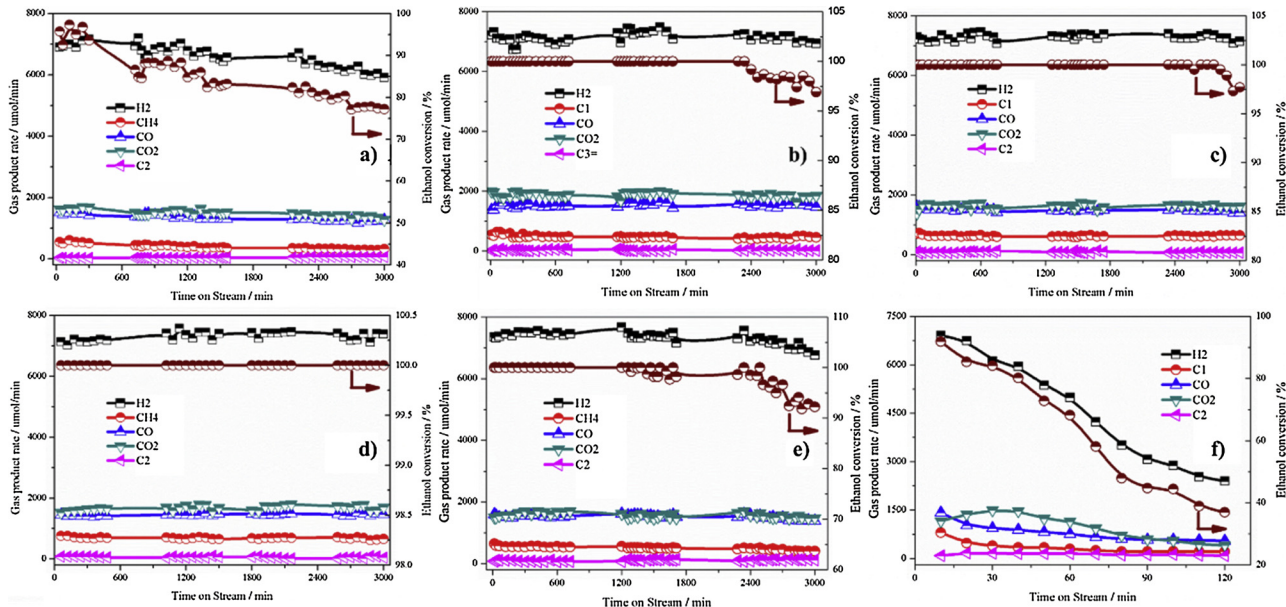


Fig. 5. The conversion of ethanol with time on stream over (a) 10Ni-CePr<sub>0</sub>, (b) 10Ni-CePr<sub>0.05</sub>, (c) 10Ni-CePr<sub>0.10</sub>, (d) 10Ni-CePr<sub>0.20</sub>, (e) 10Ni-CePr<sub>0.30</sub> and (f) 10Ni-CePr<sub>0.20</sub>-IMP. The points are the experimental data, the lines are the fitting results. Reaction conditions: T = 600 °C, H<sub>2</sub>O/C<sub>2</sub>H<sub>5</sub>OH = 4, C<sub>2</sub>H<sub>5</sub>OH-H<sub>2</sub>O GHSV = 44,240 ml/g<sub>cat</sub> h<sup>-1</sup>, P = 1 atm, N<sub>2</sub> = 60 ml/min.

0.1 (10Ni-CePr<sub>0.10</sub>), complete conversion of ethanol was retained for 2520 min, and corresponding hydrogen production rate was 7091.5 μmol/min. When 10Ni-CePr<sub>0.20</sub> was used, complete conversion of ethanol had been achieved during the whole test period (3000 min), and hydrogen production rate was as high as 7247.2 μmol/min. 10Ni-CePr<sub>0.30</sub> is a little inferior to the other three Pr-doped catalysts (10Ni-CePr<sub>0.05</sub>, 10Ni-CePr<sub>0.10</sub> and 10Ni-CePr<sub>0.20</sub>). But it still gave higher ethanol conversion and hydrogen production rate than 10Ni-CePr<sub>0</sub> without any Pr doping. The final conversion was maintained above 90% and the average hydrogen production rate was 6763.4 μmol/min after 3000 min. Wang et al. [38] reported that doped Pr<sub>2</sub>O<sub>3</sub> could highly improve the catalytic performance of Ir/CeO<sub>2</sub> for ethanol steam reforming. The high performance of Ir/CeO<sub>2</sub> was attributed to highly enhanced anti-sintering property by the fine distribution of constituents in the catalyst and effectively suppressed coke deposition by oxygen vacancies. Cristina et al. [55] showed that abundant oxygen vacancies were beneficial to the oxidation of carbonaceous species during reaction which leads to a prolonged stability of the catalyst.

10Ni-CePr<sub>0.20</sub> was further challenged in the stability test of even longer time (7200 min) as shown in Fig. S8. Compared with 10Ni-CePr<sub>0</sub> and 10Ni-CePr<sub>0.20</sub>-IMP, 10Ni-CePr<sub>0.20</sub> can efficiently convert 100% ethanol for 7200 min without any deactivation. In previous studies, various catalysts had been prepared for steam reforming of ethanol or bio-ethanol. Their catalytic performances are compared with that of our catalyst in Table 3. Under similar reaction conditions, our catalyst exhibited superior performance with very low carbon deposition and low activity loss during long-time reaction. These results suggest that 10Ni-CePr<sub>0.20</sub> developed in this work is considered as an outstanding and competitive candidate for SRE.

### 3.3. Characterization of the spent catalysts

The used catalysts that were treated in the stability tests were characterized in this section. Reaction conditions of the stability test are described in Fig. S8. XRD patterns of the spent catalysts are displayed in Fig. 6. Crystalline fluorite structure of ceria was exhibited. The main peaks became sharper and narrower compared with those of corresponding fresh catalysts. It is attributed to the sintering of the support [56]. The diffraction peak of Ni at 44.5° also became sharper and

narrower for the spent 10Ni-CePr<sub>0.20</sub>-IMP and 10Ni-CePr<sub>0</sub>. It indicates the sintering of Ni particles after long-term reaction. The sintered metal particles lead to reduced surface area of active metal, thus resulting in weakened capability towards C–C bond cleavage [27,29]. The changes are responsible for the activity loss of catalyst during ethanol conversion. While, the Ni diffraction peak at 44.5° does not change so much for the spent 10Ni-CePr<sub>0.20</sub> in comparison to corresponding fresh catalyst. The sintering of Ni particles has been efficiently suppressed by Pr doping and sol-gel preparation in severe conditions of stability test. This improvement can be explained by the increased Ni dispersion and the resulting enhanced metal-support interaction as verified by TPR (Fig. 2).

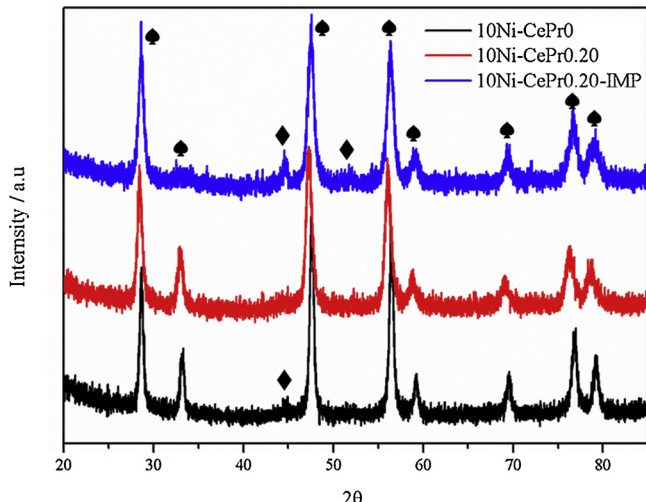
Morphology of the spent catalysts was also characterized by TEM (Fig. 7). In the spent catalysts of 10Ni-CePr<sub>0.20</sub>-IMP and 10Ni-CePr<sub>0</sub>, filamentous carbon was easily observed. Additionally, many Ni particles with larger size can be differentiated from the support in the spent 10Ni-CePr<sub>0.20</sub>-IMP (Fig. 7a and b). It means that nickel particles are apt to sinter under severe high-temperature reforming conditions in the presence of steam [41]. Moreover, graphene carbon encapsulated the nickel particles [35]. According to previous report, sintered and encapsulated nickel particles possess low capability of C–C bond cleavage [27,56]. Thus the performance of 10Ni-CePr<sub>0.20</sub>-IMP was deteriorated within only 120 min (Fig. 5 and Fig. S8). In the spent 10Ni-CePr<sub>0</sub>, the aggregation of metal Ni also existed as shown in Fig. 7c and 7d compared with corresponding fresh catalyst (Fig. S2). Filamentous carbon could obviously to be observed. The Ni particles are mainly on the tip of carbon filament which can still keep some active sites for SRE [22,59]. The conversion of ethanol continuously declined during reaction (Fig. 5 and Fig. S8). In comparison, the sintering of Ni on spent 10Ni-CePr<sub>0.20</sub> is unapparent. Ni particle size of the spent catalysts was measured and presented in Table 1. For the spent 10Ni-CePr<sub>0.20</sub>, the average size of nickel nanoparticle is only 6.2 nm. While, for the spent 10Ni-CePr<sub>0</sub> without Pr doping, the size of supported nickel nanoparticle was increased from 7.7 nm to 11.2 nm. In comparison, 10Ni-CePr<sub>0.20</sub>-IMP showed the sintered nickel nanoparticles with the size of 17.8 nm.

SEM images of the spent catalysts are shown in Fig. S9. Filamentous carbon (nanotube) was observed on all the spent catalysts. Abundant carbon nanotubes were generated in 10Ni-CePr<sub>0</sub> and 10Ni-CePr<sub>0.20</sub>-IMP after reaction as shown in Fig. S9a and S9c. While, the spent 10Ni-

**Table 3**

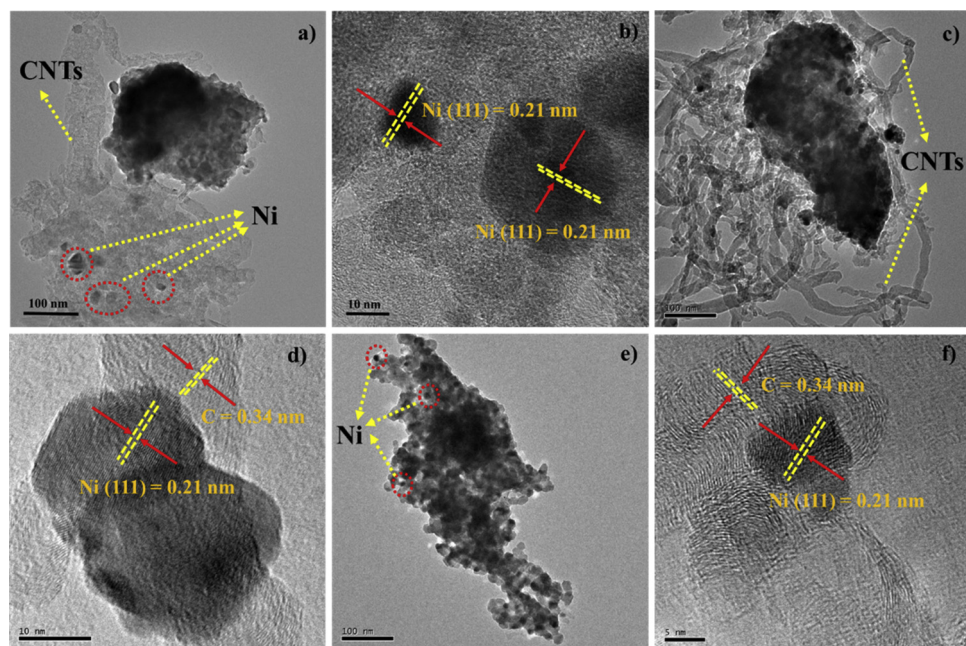
Comparison of the catalytic performances among previously reported catalysts and that developed in this work.

Ref.	Catalyst and corresponding BET surface area (m <sup>2</sup> /g)	Temperature (°C)/mole ratio of H <sub>2</sub> O/C	GHSV ml/g <sub>cat</sub> ·h (ethanol-water)	Activity loss(%) <sup>a</sup> /Reaction time /h	Carbon deposition (mg/g <sub>cat</sub> ·h)
[36]	Ni <sub>15</sub> LaSn <sub>950</sub> (62)	650/4.5	41000	1/80	0.78
[27]	1CeNi/SBA-15 (538)	650/4	57000	10/50	1.6
[28]	Ni-1Ce/MMT (67.2)	650/2	—	8.9/50	—
[29]	Meso-3LaNiAl (202)	600/2	57000	0/50	2.28
[31]	Ni-0.25Sn/CeO <sub>2</sub> (7.3)	600/5	57000	5/20	—
[12]	Ni/Ce <sub>0.8</sub> Zr <sub>0.2</sub> (85)	600/2.5	60000	10/10	27
[56]	Ni/La <sub>2</sub> O <sub>3</sub> - $\alpha$ -Al <sub>2</sub> O <sub>3</sub> (33.9)	700/6	13800	0/4	2.6
[38]	Ir/CeO <sub>2</sub> (148)	650/1.5	18000	35/300	—
[55]	Ni-Ce-La (76)	550/3	7742	10/60	1
[57]	Ni/10Mg-ATP (356.7)	700/1.5	19200	2/50	6.1
[58]	Ni/MgO (28)	650/4.2	80000	42/24	2.4
This work	10Ni-CePr <sub>0.20</sub> (26)	600/2	44240	0/120	0.56

<sup>a</sup> The initial ethanol conversion subtract final ethanol conversion.**Fig. 6.** XRD patterns of the spent catalysts. Characteristic peaks of CeO<sub>2</sub> and Ni are labeled by ◆ and ◆, respectively.

CePr<sub>0.20</sub> possessed much less coke. It indicates that effective inhibition of carbon deposition can be achieved on CeO<sub>2</sub> supported Ni by Pr doping and sol-gel preparation. These results are in good agreement with the data of XRD (Fig. 6) and TEM (Fig. 7).

In order to determine the type and the amount of coke deposited on the spent catalysts, TG and DTG were employed, and the results are shown in Fig. 8a. The rate of coke deposition was calculated and summarized in Table S5. It is verified that effective inhibition of coke deposition rate was achieved on the Ni-CeO<sub>2</sub> catalyst with suitable Pr doping prepared by sol-gel method. According to the data in Table S5, coke deposition rate on 10Ni-CePr<sub>0.20</sub>-IMP (0.131 g<sub>c</sub>/g<sub>cat</sub>·h) is more than 85 times that of 10Ni-CePr<sub>0</sub> (0.00154 g<sub>c</sub>/g<sub>cat</sub>·h). It may be attributed to more homogeneous Ni distribution in 10Ni-CePr<sub>0</sub> synthesized by sol-gel method than 10Ni-CePr<sub>0.20</sub>-IMP prepared by traditional impregnation. Large amount of deposited coke will increase the pressure drop of tubular reactor [18,59], which can explain the forced stopping of reaction over 10Ni-CePr<sub>0.20</sub>-IMP in very short time (120 min). Moreover, the coke deposition rate on was decreased to only 0.00056 g<sub>c</sub>/g<sub>cat</sub>·h over 10Ni-CePr<sub>0.20</sub>. It can be explained by the fact that the introduction of Pr into Ni-Ce solid oxide promoted metal-support interaction and generated more oxygen vacancies, which are beneficial to coke inhibition.

**Fig. 7.** TEM images of (a-b) 10Ni-CePr<sub>0.20</sub>-IMP, (c-d) 10Ni-CePr<sub>0</sub>, and (e-f) 10Ni-CePr<sub>0.20</sub> after reaction.

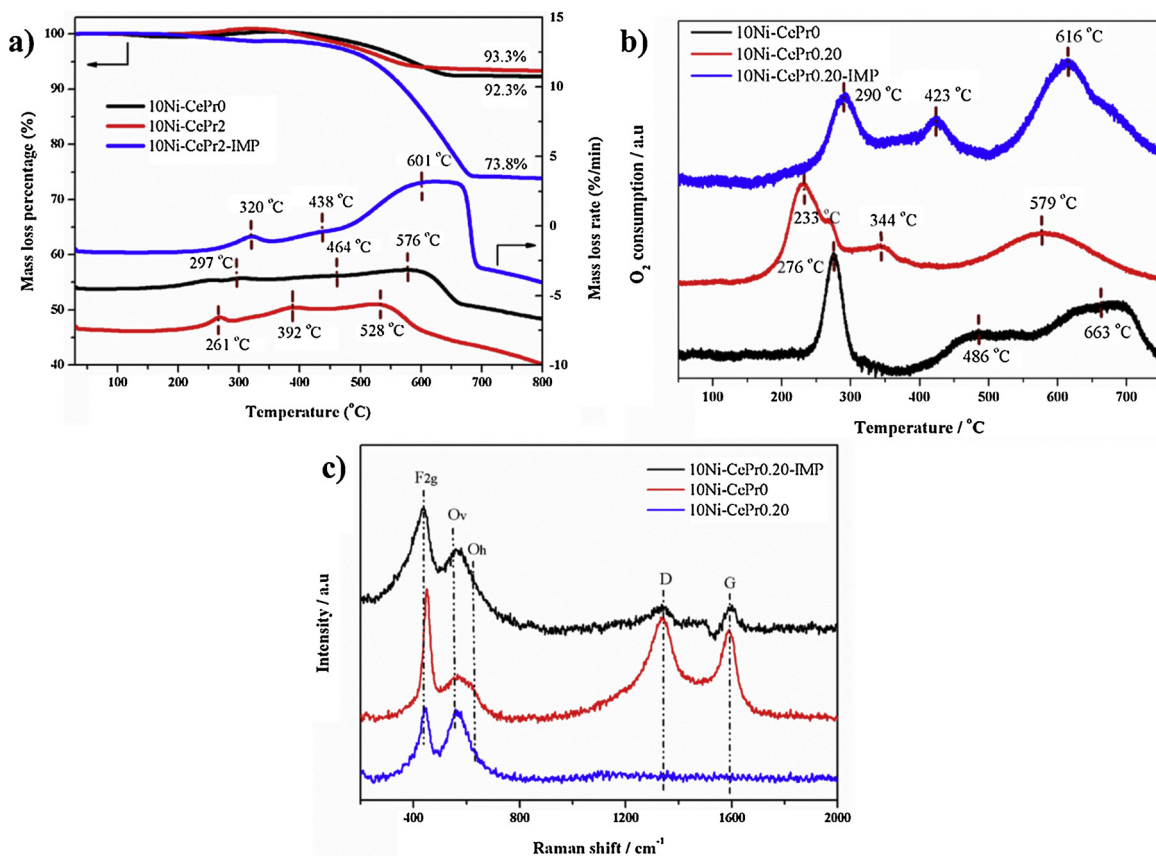


Fig. 8. (a) TG/DTG profiles, (b) O<sub>2</sub> temperature-programmed oxidation of the spent catalysts and (c) Raman profiles of the spent catalysts.

The DTG data of the spent catalysts are also shown in Fig. 8a. As illustrated in the DTG profiles, there are three kinds of deposited coke. The peak at the temperature of lower than 300 °C comes from active carbon which can be easily oxidized [27,29,33]. The two peaks at higher temperature are assigned to two different types of carbonaceous species [27]. The peak at lower temperatures (392 °C) is related to coke deposited on metal surface, and the peak at higher temperatures (528 °C) is assigned to the coke on the support. The intensities of both peaks for spent 10Ni-CePr<sub>0.20</sub> are much smaller than those of spent 10Ni-CePr<sub>0</sub> and 10Ni-CePr<sub>0.20</sub>-IMP. Specifically, some cokes deposited on 10Ni-CePr<sub>0</sub> and 10Ni-CePr<sub>0.20</sub>-IMP need higher temperature to be removed, as shown in Table S5. Coke can be easily deposited and hardly removed on 10Ni-CePr<sub>0</sub> and 10Ni-CePr<sub>0.20</sub>-IMP. Because they possess big Ni particles, weak metal-support interaction and deficient oxygen vacancies.

O<sub>2</sub> temperature-programmed oxidation (TPO) of the spent catalysts was also carried out, and the results are shown in Fig. 8b. The peak at a temperature of lower than 300 °C might be derived from the combustion of amorphous carbon species, and the peaks at higher temperatures could be attributed to the oxidation of graphitic carbon [29,60]. Furthermore, the peaks at high temperatures of 300–500 °C and 500–750 °C are further ascribed to the oxidation of coke deposited on the metal surface and the support, respectively [27]. The spent 10Ni-CePr<sub>0.20</sub> possesses smaller peak with weaker intensity at 300–500 °C compared with those of spent 10Ni-CePr<sub>0</sub> and 10Ni-CePr<sub>0.20</sub>-IMP. It indicates that less coke was deposited on Ni particles, which maintained stable performance for high ethanol conversion and hydrogen production.

Raman spectra elucidate more information on the nature of carbonaceous deposits on the spent catalysts. Fig. 8c shows the Raman spectra of the spent catalysts. Two obvious peaks are observed for the spent catalysts of 10Ni-CePr<sub>0</sub> and 10Ni-CePr<sub>0.20</sub>-IMP at around

1340 cm<sup>-1</sup> (D band) and 1580 cm<sup>-1</sup> (G band). D band is ascribed to the disorder or defects induced by the structural imperfections, which exists in defective carbonaceous materials [61]. Whereas G band is related with the in plane C–C stretching vibrations of all pairs of sp<sup>2</sup> atoms in graphite layers. The observed relatively strong intensity of the D band to the G band suggests the presence of more disordered carbonaceous species than graphitic carbon on the catalysts. For the spent 10Ni-CePr<sub>0.20</sub>, both D band and G band were not observed. It indicates that the amount of coke deposited on 10Ni-CePr<sub>0.20</sub> is tiny compared with those on 10Ni-CePr<sub>0</sub> and 10Ni-CePr<sub>0.20</sub>-IMP. These results are consistent with the conclusions based on TEM (Fig. 7), SEM (Fig. S9) and TG/DTG (Fig. 8a). Besides the carbon peak in Raman spectra, the peaks of F<sub>2g</sub>, O<sub>v</sub> and O<sub>h</sub> indicating the structure of ceria could also to be clearly observed. Slight red shift of F<sub>2g</sub>, O<sub>v</sub> and O<sub>h</sub> peaks for Pr-doped samples (10Ni-CePr<sub>0.20</sub> and 10Ni-CePr<sub>0.20</sub>-IMP) compared the sample without any Pr (10Ni-CePr<sub>0</sub>) can be found, which is similar to that observed in fresh samples (Fig. 3a). It further confirmed the doping of Pr into ceria lattice. As shown in Fig. 8c, after long-time stability test under severe conditions, the peak intensity of O<sub>v</sub> and O<sub>h</sub> for Pr-doped samples was still very high. The values of (O<sub>v</sub> + O<sub>h</sub>)/F<sub>2g</sub> for the spent catalysts were calculated and summarized in Table S4. (O<sub>v</sub> + O<sub>h</sub>)/F<sub>2g</sub> is in the order of 10Ni-CePr<sub>0.20</sub> (1.520) > 10Ni-CePr<sub>0.20</sub>-IMP (0.940) > 10Ni-CePr<sub>0</sub> (0.920). Compared with (O<sub>v</sub> + O<sub>h</sub>)/F<sub>2g</sub> for the fresh 10Ni-CePr<sub>0.20</sub>-IMP (1.588), the value of (O<sub>v</sub> + O<sub>h</sub>)/F<sub>2g</sub> for the spent 10Ni-CePr<sub>0.20</sub>-IMP was decreased by 0.648. This is attributed to the sintering of catalyst at high temperature during long-time reaction, which is also confirmed by XRD (Fig. 6) and TEM (Fig. 7). For the sample prepared by sol-gel method with suitable Pr doping, the value of (O<sub>v</sub> + O<sub>h</sub>)/F<sub>2g</sub> was only slightly reduced from 1.704 to 1.52.

Combining the results of XRD (Fig. 6), TEM (Fig. 7), SEM (Fig. S9), TG (Fig. 8a), TPO (Fig. 8b) and Raman spectra (Fig. 8c), it can be concluded that Ni sintering and coke deposition of CeO<sub>2</sub> supported Ni

have been greatly suppressed by both Pr doping and the sol-gel preparation. The high performance of  $10\text{Ni-CePr}_x$  solid oxides developed in this work is derived from its well-controlled structure with great improvements in three aspects. First, the sol-gel method employed in catalyst preparation effectively reduces Ni particle size and facilitates Ni dispersion, as verified by XRD (Fig. 1), TPR (Fig. 2) and TEM (Fig. S2 and S3). Second, the doping of suitable amount of Pr significantly increases oxygen vacancies in the catalyst as confirmed by Raman (Fig. 3a), EPR (Fig. 3b), XPS (Fig. S4c) and DFT calculations (Fig. 4). Third, properly doped Pr also enhances metal-support interaction as shown in TPR (Fig. 2). As a result, effective anti-sintering and coke suppression has been achieved during long-time SRE with high capacities of ethanol conversion and  $\text{H}_2$  generation under severe conditions, as demonstrated by the results of XRD (Fig. 6), TEM (Fig. 7), SEM (Fig. S9), TG (Fig. 8a), TPO (Fig. 8b) and Raman spectra (Fig. 8c).  $10\text{Ni-CePr}_{0.20}\text{-IMP}$  with big Ni particles and low oxygen vacancy concentration possesses low ability to activate water [18,38] which makes the gasification of deposited coke hardly proceeds. The growing of carbon nanotubes or carbon fibers under Ni particles on the surface causes Ni particles to be apart from the support. The SRE activity over  $10\text{Ni-CePr}_{0.20}\text{-IMP}$  sharply decreased in short period of time. In comparison,  $10\text{Ni-CePr}_{0.20}$  with highly dispersed Ni particles, enhanced metal-support interaction and abundant oxygen vacancies is active and stable in SRE (Fig. S8).

#### 4. Conclusions

To summarize, various Pr-doped ceria supported Ni catalysts ( $10\text{Ni-CePr}_x$ ) have been synthesized via a sol-gel method and applied in ethanol steam reforming. Different techniques including XRD,  $\text{N}_2$  adsorption-desorption,  $\text{H}_2$ -TPR,  $\text{H}_2$  chemisorption, Raman, XPS, TEM, TG and TPO were used to characterize the fresh and spent catalysts. The results showed that the sol-gel method can effectively increase Ni dispersion and enhance metal-support interaction compared with traditional impregnation method. Pr doping can further control the size of Ni particles via affecting metal-support interaction. Properly doping of Pr into ceria for the loading of Ni by the sol-gel method led to highly active SRE catalysts with excellent anti-sintering performance. Moreover, the concentration of oxygen vacancies was increased by Pr doping, which effectively inhibited coke deposition. DFT calculations further revealed the origin of abundant oxygen vacancies in Pr-doped ceria supported Ni. The formation energy of oxygen vacancy in Ni and Pr co-doped ceria is as low as -1.39 eV. Consequently, the catalyst of  $10\text{Ni-CePr}_{0.20}$  exhibited superior activity and stability, on which complete conversion of ethanol can be maintained for more than 7200 min.  $10\text{Ni-CePr}_{0.2}\text{-IMP}$  prepared by the impregnation method lost its activity after only 120 min. On  $10\text{Ni-CePr}_0$  the conversion of ethanol dropped to 77.2% after 3000 min. The coke deposition rate on  $10\text{Ni-CePr}_{0.20}$  is only 0.00056  $\text{g}_c/\text{g}_{\text{cat}}\text{h}$ , which are 0.131  $\text{g}_c/\text{g}_{\text{cat}}\text{h}$  and 0.00154  $\text{g}_c/\text{g}_{\text{cat}}\text{h}$  on  $10\text{Ni-CePr}_{0.20}\text{-IMP}$  and  $10\text{Ni-CePr}_0$ , respectively.

#### Declaration of Competing Interest

The authors declare that they have no known competing financial interests or personal relationships that could have appeared to influence the work reported in this paper.

#### Acknowledgements

The authors gratefully acknowledge financial support from the National Key Research and Development Program of China (2016YFB0600305) and the National Natural Science Foundation of China (21306132, 21476168). The calculations were performed on TianHe-1(A) at National Supercomputer Center in Tianjin. The author would like to thank Dr. Kui Ma and Dr. Guoqiang Shen for helpful discussion.

#### Appendix A. Supplementary data

Supplementary material related to this article can be found, in the online version, at doi:<https://doi.org/10.1016/j.apcatb.2019.117940>.

#### References

- [1] O.O. James, S. Maity, M.A. Mesubi, K.O. Ogunniran, T.O. Siyanbola, S. Sahu, R. Chaubey, *Green Chem.* 13 (2011) 2272–2284.
- [2] S. Zhan, H. Zhang, Y. Zhang, Q. Shi, Y. Li, X. Li, *Appl. Catal. B* 203 (2017) 199–209.
- [3] A.J. Vizcaíno, A. Carrero, J.A. Calles, *Int. J. Hydrogen Energy* 32 (2007) 1450–1461.
- [4] L. Lin, W. Zhou, R. Gao, S. Yao, X. Zhang, W. Xu, S. Zheng, Z. Jiang, Q. Yu, Y.W. Li, C. Shi, X.D. Wen, D. Ma, *Nature* 544 (2017) 80–83.
- [5] H.-M. Kim, W.-J. Jang, S.-Y. Yoo, J.-O. Shim, K.-W. Jeon, H.-S. Na, Y.-L. Lee, B.-H. Jeon, J.W. Bae, H.-S. Roh, *Int. J. Hydrogen Energy* 43 (2018) 262–270.
- [6] D. Li, X. Li, J. Gong, *Chem. Rev.* 116 (2016) 11529–11653.
- [7] Y.C. Sharma, A. Kumar, R. Prasad, S.N. Upadhyay, *Renewable Sustainable Energy Rev.* 74 (2017) 89–103.
- [8] J. Sun, Y. Wang, *ACS Catal.* 4 (2014) 1078–1090.
- [9] D. Zanchet, J.B.O. Santos, S. Damyanova, J.M.R. Gallo, J.M.C. Bueno, *ACS Catal.* 5 (2015) 3841–3863.
- [10] T. Hou, S. Zhang, Y. Chen, D. Wang, W. Cai, *Renewable Sustainable Energy Rev.* 44 (2015) 132–148.
- [11] T.S. Moraes, R.C. Rabelo Neto, M.C. Ribeiro, L.V. Mattos, M. Kourtelesis, S. Ladas, X. Verykios, F.B. Noronha, *Appl. Catal. B* 181 (2016) 754–768.
- [12] I.A. Carbajal-Ramos, M.F. Gomez, A.M. Condó, S. Bengió, J.J. Andrade-Gamboa, M.C. Abello, F.C. Gennari, *Appl. Catal. B* 181 (2016) 58–70.
- [13] J. Pu, K. Nishikado, N. Wang, T.T. Nguyen, T. Maki, E.W. Qian, *Appl. Catal. B* 224 (2018) 69–79.
- [14] G. Zhou, L. Barrio, S. Agnoli, S.D. Senanayake, J. Evans, A. Kubacka, M. Estrella, J.C. Hanson, A. Martinez-Arias, M. Fernandez-Garcia, J.A. Rodriguez, *Angew. Chemie* 49 (2010) 9680–9684.
- [15] S. Zhang, S. Muratsugu, N. Ishiguro, M. Tada, *ACS Catal.* 3 (2013) 1855–1864.
- [16] G. Wu, S. Li, C. Zhang, T. Wang, J. Gong, *Appl. Catal. B* 144 (2014) 277–285.
- [17] Z. Li, L. Mo, Y. Kathiraser, S. Kawi, *ACS Catal.* 4 (2014) 1526–1536.
- [18] D. Li, M. Koike, J. Chen, Y. Nakagawa, K. Tomishige, *Int. J. Hydrogen Energy* 39 (2014) 10959–10970.
- [19] J. Sehested, *Catal. Today* 111 (2006) 103–110.
- [20] L.-C. Chen, S.D. Lin, *Appl. Catal. B* 106 (2011) 639–649.
- [21] B.P.S. Damyanova, R. Palcheva, Y. Karakirova, M.C. Capel Sanchez, G. Tyuliev, E. Gaigneaux, J.L.G. Fierro, *Appl. Catal. B* 225 (2018) 340–353.
- [22] C.J. Liu, J. Ye, J. Jiang, Y. Pan, *Chemcatchem* 42 (2011) 529–541.
- [23] S. Li, J. Gong, *Chem. Soc. Rev.* 43 (2014) 7245–7256.
- [24] D.L.D. Javier Carrasco, Zongyuan Liu, Tomas Duchon, Jaime Evans, Sanjaya D. Senanayake, Ethan J. Crumlin, Vladimir Matolim, Jose A. Rodriguez, M. Veronica Ganduglia-Pirovano, *Angew. Chem.* 127 (2015) 3989–3993.
- [25] K. Kamonsuangsaksem, S. Therdthianwong, A. Therdthianwong, N. Thammajak, *Appl. Catal. B* 218 (2017) 650–663.
- [26] D. Kim, B.S. Kwak, B.-K. Min, M. Kang, *Appl. Surf. Sci.* 332 (2015) 736–746.
- [27] D. Li, L. Zeng, X. Li, X. Wang, H. Ma, S. Assabumrungrat, J. Gong, *Appl. Catal. B* 176–177 (2015) 532–541.
- [28] L. Li, D. Tang, Y. Song, B. Jiang, Q. Zhang, *Energy* 149 (2018) 937–943.
- [29] H. Ma, L. Zeng, H. Tian, D. Li, X. Wang, X. Li, J. Gong, *Appl. Catal. B* 181 (2016) 321–331.
- [30] P. Osorio-Vargas, N.A. Flores-González, R.M. Navarro, J.L.G. Fierro, C.H. Campos, P. Reyes, *Catal. Today* 259 (2016) 27–38.
- [31] L.X. Tian Hao, Chen Sai, Zeng Liang, Gong Jinlong, *Chinese J. Chem.* 35 (2017) 651–658.
- [32] A.H. Eranda Nikolla, Johannes Schwank, Suljo Linic, *J. Am. Chem. Soc.* 128 (2006) 11354–11355.
- [33] Z. Xiao, C. Wu, L. Li, G. Li, G. Liu, L. Wang, *Int. J. Hydrogen Energy* 42 (2017) 5606–5618.
- [34] N. Wang, K. Shen, L. Huang, X. Yu, W. Qian, W. Chu, *ACS Catal.* 3 (2013) 1638–1651.
- [35] H. Muroyama, R. Nakase, T. Matsui, K. Eguchi, *Int. J. Hydrogen Energy* 35 (2010) 1575–1581.
- [36] J. Bussi, M. Musso, A. Quevedo, R. Faccio, M. Romero, *Catal. Today* 296 (2017) 154–162.
- [37] Z. Xiao, S. Ji, F. Hou, Y. Li, H. Zhang, L. Wang, X. Zhang, G. Liu, J. Zou, G. Li, *Catal. Today* 316 (2018) 78–90.
- [38] W.C. Fagen Wang, H.élene Provendier, Yves Schuurman, Claude Descorme, Claude Mirodatos, Wenjie Shen, *Int. J. Hydrogen Energy* 36 (2011) 13566–13574.
- [39] U. Oemar, P.S. Ang, K. Hidajat, S. Kawi, *Int. J. Hydrogen Energy* 38 (2013) 5525–5534.
- [40] S. Fabris, S.D. Gironcoli, S. Baroni, G. Vicario, G. Balducci, *Phys. Rev. B* 71 (2005) 041102(041101–041104).
- [41] J.C. Ying Chen, P. Hu, Haifeng Wang, *Surf. Sci.* 602 (2008) 2828–2834.
- [42] A.J. Delfina Garcí a Pintos, Beatriz Irigoyen, *Int. J. Hydrogen Energy* 37 (2012) 14937–14944.
- [43] A.J. Brian Milberg, Beatriz Irigoyen, *Appl. Surf. Sci.* 401 (2017) 206–217.
- [44] M.Sa.T. Ziegler, *J. Phys. Chem. C* 114 (2010) 21411–21416.
- [45] S. Xu, X. Yan, X. Wang, *Fuel* 85 (2006) 2243–2247.
- [46] R.K. Singha, A. Shukla, A. Yadav, L.N. Sivakumar Konathala, R. Bal, *Appl. Catal. B*

202 (2017) 473–488.

[47] L. Pino, A. Vita, F. Cipiti, M. Laganà, V. Recupero, *Catal. Letters* 122 (2007) 121–130.

[48] S. Mahammadunnisa, P. Manoj Kumar Reddy, N. Lingaiah, C. Subrahmanyam, *Catal. Sci. Technol.* 3 (2013) 730–736.

[49] D. Harshini, D.H. Lee, J. Jeong, Y. Kim, S.W. Nam, H.C. Ham, J.H. Han, T.-H. Lim, C.W. Yoon, *Appl. Catal. B* 148–149 (2014) 415–423.

[50] G.H. Youjin Lee, Austin J. Akey, Rui Si, Maria Flytzani-Stephanopoulos, Irving P. Herman, *J. Am. Chem. Soc.* 133 (2011) 12952–12955.

[51] G. Niu, E. Hildebrandt, M.A. Schubert, F. Boscherini, M.H. Zoellner, L. Alff, D. Walczyk, P. Zaumseil, I. Costina, H. Wilkens, *ACS Appl. Mater. Interfaces* 6 (2014) 17496–17505.

[52] M.A. Malecka, L. Kepiński, W. Miśta, *Appl. Catal. B* 74 (2007) 290–298.

[53] D. Chen, D. He, J. Lu, L. Zhong, F. Liu, J. Liu, J. Yu, G. Wan, S. He, Y. Luo, *Appl. Catal. B* 218 (2017) 249–259.

[54] Yong-Chao Zhang, Lei Zhang, Lun Pan, Xiangwen Zhang, Li Wang, Ji-Jun Zou Fazal-e-Aleem, *Appl. Catal. B* 224 (2018) 101–108.

[55] F.M. Cristina Pizzolitto, Elena Ghedini, Giada Innocenti, Alessandro Di Michele, Giuseppe Cruciani, Fabrizio Cavani, Michela Signoretto, *ACS Sustain. Chem. Eng.* (2018).

[56] B. Valle, B. Aramburu, A. Remiro, J. Bilbao, A.G. Gayubo, *Appl. Catal. B* 147 (2014) 402–410.

[57] M. Chen, Y. Wang, Z. Yang, T. Liang, S. Liu, Z. Zhou, X. Li, *Fuel* 220 (2018) 32–46.

[58] S. Freni, S. Cavallaro, N. Mondello, L. Spadaro, F. Frusteri, *Catal. Commun.* 4 (2003) 259–268.

[59] X. Zhu, P. Huo, Y.-P. Zhang, D.-G. Cheng, C.-J. Liu, *Appl. Catal. B* 81 (2008) 132–140.

[60] Z. Xiao, L. Li, C. Wu, G. Li, G. Liu, L. Wang, *Catal. Letters* 146 (2016) 1–12.

[61] I.H. Son, S.J. Lee, I.Y. Song, W.S. Jeon, I. Jung, D.J. Yun, D.W. Jeong, J.O. Shim, W.J. Jang, H.S. Roh, *Fuel* 136 (2014) 194–200.